STRAIN HARDENING AND DISLOCATION AVALANCHES IN MICROMETER-SIZED DIMENSIONS

Jorge Alcalá[1], Jan Očenášek[2], Kai Nowag[3], Daniel Esqué-de los Ojos[3], Rudy Ghisleni[3], Johann Michler[3]

[1]Department of Materials Science and Metallurgical Engineering, GRICCA. EUETIB and ETSEIB. Universitat Politècnica de Catalunya, 08028 Barcelona, Spain.

[2]New Technologies Research Centre, University of West Bohemia in Pilsen, 30614 Plzeň, Czech Republic.

[3]Laboratory for Mechanics of Materials and Nanostructures, EMPA: Swiss Federal Laboratories for Materials Science and Technology, 3602 Thun, Switzerland.

Abstract

Present experiments and computational simulations furnish a fundamental background to the understanding of plastic flow across sample sizes. It is shown that self-organized criticality (SOC) governs the size distribution of dislocation avalanches in micrometer-sized sample dimensions. Onset of SOC denotes inception of a dislocation network so that dislocation avalanches occur at constant criticality level irrespectively of the applied stress. In these microcrystals, we find that the ratio between the characteristic sample dimension and the mean free path travelled by the mobile dislocations, D/L_{eff}, rules onset of strain hardening. This index simultaneously accounts for the role of loading orientation and dislocation density upon microscale plasticity. It is shown that strain-hardening emerges for $D/L_{eff} > 2$, where surface dislocation annihilations are inconsequential to network development and the flow stress scales with dislocation density. This regime naturally evolves towards bulk plasticity at increasing sample sizes. Conversely, strain hardening is suppressed when confining sample dimensions dominate plastic flow for $D/L_{eff} < 1.5$. Confining microscale plasticity is characterized by a significant increase in the size of dislocation avalanches under a stagnant dislocation network.

Keywords: Crystal plasticity, mechanical properties, dislocations, strain hardening.

Submitted to **Acta Materialia**

August 2014

1. Introduction

Strain hardening is a distinctive feature in crystal plasticity, where the flow stress increases during load application due to the development of an entangled dislocation network [1—3]. The physical underpinning between plastic flow and the increase in dislocation density is however absent in submicrometer-sized crystals where dislocation annihilations at the free surface limits dislocation storage [4—6]. In such confining sample sizes, sudden activation and deactivation of surface-truncated (single-ended) dislocation sources under increasing applied stresses produces an intermittent supply of mobile dislocation segments. As such source-exhaustion hardening mechanisms come into play, the stress—strain curve is found to exhibit marked plastic bursts [7—9].

A central aspect in the understanding of crystal plasticity concerns assessment of the transition between confining and bulk plastic flow [10—13]. This is a complex issue to analyze because of the vast dislocation density arising in micrometer-sized samples [13] and its sensitivity to loading orientation. Onset of bulk strain hardening would be therefore facilitated in dislocation networks arising under such multiple-glide loading orientations that exhibit strong dislocation interactions and storage. Surface dislocation annihilations and the emergence of confining plasticity would then be enhanced in multiple or single glide orientations where milder dislocation interactions occur.

The fundamental discreteness of crystal plasticity is due to the onset of dislocation avalanches. Mean-field statistical analyses indicate that the probability density of dislocation avalanche slips fulfills a universal power-law (scale-invariant) form similar to that describing other physical instabilities such as earthquakes in fault systems [14—17]. Knowledge is however unavailable on whether transition from bulk to confining plasticity fundamentally affects avalanche development.

The following are the main purposes for this investigation. First, we seek to provide a thorough analysis to the emergence of strain hardening in small sample dimensions. Mean-field (continuum) crystal plasticity is central to this work, as the behavior of a random dislocation population is averaged using uniform dislocation densities. Whereas a preconceived idea appears to be that such analyses may not hold in microscopic crystals [12, 18, 19], our experiments show that a deterministic understanding to microscale plasticity and its evolution across sample dimensions becomes accessible through this scheme. Secondly, it is our purpose to furnish experimental evidence on the influence of strain hardening upon the size distribution of dislocation avalanches. This investigation therefore provides a solid mean-field mechanical and statistical comprehension to the evolution of plasticity across sample dimensions.

2. Uniaxial stress—strain curves and the counting of dislocation avalanches

Present investigation comprises 40 micropillar compression experiments performed in copper single crystals with diameters D = 1.2, 2.0, 7.0 and 20 μm and aspect ratio (diameter:length) of 1:3. The micropillars were manufactured by Focused Ion Beam (FIB) milling from (i) a well-annealed copper single crystal with the <111> orientation and (ii) single grains with the <012> and <001> orientations –as measured by Electron Back-Scatter Diffraction (EBSD)– from a polycrystalline copper sample. This polycrystalline sample had been previously heat-treated in vacuum to obtain substantial grain growth to a final average size of 30 μm. During machining, FIB energy was set at 30 KeV while a low value of 180 pA was selected for the beam current in the final step. The load—displacement curves were recorded using an in-house system operating in true displacement (strain) control inside the chamber of a Scanning Electron Microscope (SEM). This allows for unique assessments of dislocation avalanches. The

imposed displacement rate was set to 2 nm/s in all experiments. Representative uniaxial stress—strain curves are shown in Figs. 1 (a) and (b).

Plastic intermittencies produced at an externally applied strain-rate of $\approx 4 \times 10^{-4}$ s^{-1} are illustrated in the highly magnified portions of the stress—strain curves in Fig. 2. Uniaxial displacements Δu_i containing a number of stress serrations (where each serration is associated with an individual dislocation avalanche) are shown in Fig. 2(a). One such plastic displacement Δu is characterized in that the applied stress remains below its initial level as marked by the arrows in Fig. 2(a). In the absence of strain-rate effects, this is equivalent to a plastic intermittency produced in more conventional experiments driven under load (stress) control. The associated slip is then given by

$$s_\sigma = {\Delta u}/{\mathrm{SF}} \quad , \tag{1}$$

where SF is the Schmid factor in the active slip systems.

Fig. 2(b) shows slip s_ε produced by an individual dislocation avalanche. The avalanche is characterized by stress serration $\Delta\sigma = \sigma_{\max} - \sigma_{\min}$ and by plastic displacement Δu accumulating along the pillar length l. Since $s_\varepsilon \times \mathrm{SF}/l$ is the accumulated uniaxial plastic strain $\Delta\varepsilon$, which necessarily equals $\Delta\sigma/E$, it follows that

$$s_\varepsilon = Nb = l\ \Delta\sigma\ /(E \times \mathrm{SF}) \quad , \tag{2}$$

where N is the number of dislocations contained in the avalanche, b is the magnitude of the Burgers vector and E is the elastic stiffness of the compressed micropillar.

Experimental fluctuations during testing translate into an uncertainty of $\Delta\sigma$ = 1 MPa. Current statistical analyses of dislocation avalanches are performed with an uncertainty stress threshold $\Delta\sigma$ that is three times greater, so that the size of the minimum discernable slip becomes s_ε = 1.86b, 1.43b and 1.84b for the <111>, <012> and <001> pillar orientations, respectively (Eq. (2)).

3. Theoretical background and mean-field models

3.1. Bulk crystal plasticity and the mean free path travelled by dislocations

Continuum descriptions of crystal plasticity allow prediction of the stress—strain curves in bulk single crystals. Advanced models are based on detailed knowledge of short-range stresses that govern junction formation [20, 21]. Short-range interactions are smoothened in space so that the critical shear stress τ^{α} for dislocation mobilization in any arbitrary slip system α scales with the forest dislocation density ρ^{β} (length of dislocation lines per unit volume) in all interacting slip systems β. This is expressed by

$$\tau^{\alpha} = \mu b \sqrt{\sum\nolimits_{\beta} a_{\alpha\beta}\, \rho^{\beta}} \quad , \tag{3}$$

where α and β run from 1 to 12 to account for all slip systems in fcc crystals, $a_{\alpha\beta}$ is a matrix prescribing Cottrell-Lomer, collinear, coplanar, glissile and Hirth dislocation interactions from discrete dislocation dynamics (DDD) simulations [20, 21] and μ is the shear modulus. The slip system combinations that produce the above interactions are given in [22]. The influence of dislocation density in matrix $a_{\alpha\beta}$ is then written as [21]

$$a_{\alpha\beta} = a_{\alpha\beta,ref} \left(\frac{\log 1/b \sqrt{\bar{a}\, \rho^{\beta}}}{\log 1/b \sqrt{\bar{a}\, \rho_{ref}}} \right) \tag{4}$$

where $\sqrt{\bar{a}} = 0.35$ and coefficients $a_{\alpha\beta,ref}$ are given in Table 1.

The essential strain hardening mechanism elucidated from DDD simulations in pure crystals is that a dislocation lying in slip system α becomes immobile because of junction zipping processes with the interacting (forest) dislocations. The dislocation is then mobilized with increasing stress through junction unzipping. Parameter L_{eff} measures the effective mean free path swept by the mobile segment during its free flight

in subsequent stages of mobilization and arrest. L_{eff} decreases with plastic straining in accordance with the classical dislocation-storage law [3]

$$\frac{d\rho^{\alpha}}{d\gamma^{\alpha}} = \frac{1}{b}\left(\frac{1}{L_{eff}}\right) \quad , \tag{5}$$

where $d\gamma^{\alpha}$ is the shear strain increment in system α and $d\rho^{\alpha}$ is the increment of dislocation density associated with the junction forming processes.

Coarse-graining of DDD simulations has recently provided a detailed model for the evolution of the mean free path length L_{eff} during plastic straining [20, 21], where

$$\frac{1}{L_{eff}} = \frac{1}{L_{jct}} + \frac{\sqrt{a_o \rho^{\alpha}}}{K_o} + \frac{\sum_{\beta c}\sqrt{a_c \rho^{\beta c}}}{K_c} \quad , \tag{6}$$

In Eq. (6) L_{jct} accounts for the different Lomer, glissile, Hirth and collinear dislocation interactions with the forest β systems; subscripts *o* and *c* indicate self ($\alpha = \beta$) and coplanar interactions, respectively; superscript βc refers to specific slip systems producing coplanar interactions with the primary α system; and *K* and *a* are the dislocation interaction coefficients. Parameter L_{jct} is given by

$$\frac{1}{L_{jct}} = \frac{p_o k_o}{\sqrt{\sum_{\beta} a_{\alpha\beta}\left(\rho^{\beta} + \rho_{jct}^{\alpha}\right)}}\left(\frac{\rho^{\alpha}}{\rho^{\alpha} + \rho_{jct}^{\alpha}}\right)\left(\sum\nolimits_{\beta}\sqrt{a_{\alpha\beta}}\rho^{\beta}\right)\left(1 - \frac{\rho_{jct}^{\alpha}}{\rho^{\beta}}\right) \quad , \tag{7}$$

where the evolution of the junction density stored in system α becomes

$$d\rho_{jct}^{\alpha} = \kappa_o \frac{p_o k_o}{b}\frac{\rho^{\alpha}\sum_{\beta}\sqrt{a_{\alpha\beta}}d\gamma^{\beta}}{\sqrt{\sum_{\beta} a_{\alpha\beta}(\rho^{\beta} + \rho_{jct}^{\beta})}}\left(1 - \frac{\rho_{jct}^{\alpha}}{(n-1)\rho^{\alpha}}\right) \quad , \tag{8}$$

n is the number of active systems, and p_o, k_o and k_o are dimensionless constants ruling junction properties (Table 1).

Notice that the above model exclusively relies on the fundamentals of junction zipping and unzipping phenomena from DDD simulations. It is therefore explicitly assumed that

strain hardening is not affected by the onset of substructural dislocation arrangements or patterning. This simplification is supported by Ref. [23], where Eq. (3) emerges from experiments irrespectively of dislocation patterning.

Under the framework of continuum crystal plasticity [24], plastic deformations are in accordance with

$$\dot{\mathbf{F}} \cdot \mathbf{F}^{-1} = \sum_{\alpha} \mathrm{d}\gamma^{\alpha}\, \mathbf{s}^{\alpha} \otimes \mathbf{m}^{\alpha} \quad , \tag{9}$$

where $\dot{\mathbf{F}}$ is the rate of the deformation gradient tensor $\mathbf{F}$, and $\mathbf{s}^{\alpha}$ and $\mathbf{m}^{\alpha}$ are the normalized vectors prescribing the slip direction and the slip plane, respectively. The Lagrangian finite-strain tensor $\boldsymbol{\varepsilon}$ is then constructed as

$$\boldsymbol{\varepsilon} = \frac{1}{2}(\mathbf{F}^{\mathrm{T}} \cdot \mathbf{F} - \mathbf{I}) \quad , \tag{10}$$

where superscript T denotes the transposed of the tensor and $\mathbf{I}$ is the unit tensor.

3.2. Statistical analyses for the size distribution of dislocation avalanches

Mean-field analyses indicate that the probability density P of slips s carried by dislocation avalanches follows scale-invariant form $P \sim s^{-1.5}$ in crystals strained above 10^{-4} s^{-1} where slow relaxation process can be neglected [14—16, 25—29]. The probability density then exhibits a cut-off at a maximum avalanche slip $s_{\max}$ that depends on crystal size. Both of these features are captured through

$$P(s) \sim s^{-1.5} \exp\left[s\,(\tau^{*} - \tau)^{2}\right] \quad , \tag{11}$$

where $s_{\max} \sim (\tau^{*} - \tau)^{-2}$, τ is the applied stress and τ^{*} is the criticality stress level in the crystal [16, 17, 27]. The concept of stress tuned criticality (STC) therefore arises as $s_{\max}$ increases when τ approaches τ^{*} [17]. Continuum dislocation theory and DDD simulations support Eq. (11) in the absence of dislocation storage, where τ^{*} thus assimilates to the yield stress [27]. The simulations further show that τ^{*} decreases with

increasing crystal size. At constant applied stress τ, such size effects result in a raise of $s_{\max}$ because of the associated decrease in the magnitude of $(\tau^* - \tau)$.

A corollary from Eq. (11) is that the complementary cumulative distribution function of avalanche slips $C(s)$ –the fraction of avalanches with slip greater than s plotted in terms of s– is binned by stress [16, 27]. Hence, function $C(s)$ spreads out depending on the applied stress τ. The stress-integrated complementary cumulative distribution $C(s)_{\text{int}}$ is however independent of stress and fulfills $C(s)_{\text{int}} \sim s^{-1}$ [16, 27]. Recent experimental measurements in submicrometer-sized pillars [16] have confirmed the stress binning of $C(s)$ as well as the relationship $C(s)_{\text{int}} \sim s^{-1}$, thus supporting the fundamental conception in that plastic intermittencies are tuned by stress (Eq. (11)).

In addition to the above analyses, the following relation has been used to model the distribution of slips with characteristic maximum size $s_{\max}$ (e.g., see [15, 28])

$$P(s) \sim s^{-1.5} \exp\left[-\left(s/s_{\max}\right)^2\right] \quad . \tag{12}$$

The conception in that $s_{\max}$ is independent of stress arises when Eq. (12) is invoked in the context of self-organized criticality (SOC), where the crystal spontaneously evolves towards a critical state with characteristic slip $s_{\max}$ [30, 31]. This theory fundamentally contradicts STC. Finally, according to the SOC analyses in [15], $s_{\max}$ would mildly depend on the slope θ of the stress—strain curve in the general case when $\theta \ll E$.

4. Correlation between experiments and mean-field analyses

4.1. Experimental assertions of strain hardening

The experimentally measured stress—strain curves in Fig. 1 show development of an incipient plasticity stage for $\tau_o < \tau < \tau_c$. The stress level at the onset of plastic flow

follows $\tau_o \propto D^{-m}$ with $m \approx 0.35$. Exponent m was found to increase towards ≈ 0.6 when the flow stress τ_o was measured at a uniaxial strain $\varepsilon = 3\%$ [13].

For <111> micropillars with $D \geq 2$ μm (Fig. 1(a)), the subsequent (generalized) plastic flow attaining at $\tau > \tau_c$ is indicative of net dislocation storage as the stress—strain curves averaged over a number of stress serrations exhibit sustained hardening ($\theta = \mathrm{d}\sigma/\mathrm{d}\epsilon > 0$). This interpretation is in accordance with the DDD simulations in [32] for microcrystals with $D > 1$ μm, as source-exhaustion hardening in the absence of dislocation storage produces pronounced hardening saturation ($\theta \to 0$).

From the above, it stems that dislocation storage during generalized plastic flow necessarily requires onset of a dense dislocation network within the incipient plasticity stage ($\tau_o < \tau < \tau_c$) through simultaneous activations of multiple truncated sources. Insufficient dislocation storage consequently emanates from the shape of the stress—strain curves in Fig. 1(b), where the flow stress fluctuates about a constant level.

4.2 Assessing slip system activity

This section describes a method to assess slip system activity in micropillar compression experiments. The method employs EBSD measurements of the plastic distortion in the top surface of compressed micropillars (Figs. 3 and 4).

For a given micropillar orientation, we start by assuming a fixed $\mathrm{d}\gamma^{\alpha} < 1 \times 10^{-4}$ in a postulated set of active slip systems. Eq. (9) is then solved yielding deformation gradient tensor **F** for each given γ^{α} level. The individual components of this tensor enable mapping of the material points in the cross-section into their final position at any uniaxial strain level. Agreement between the computed and experimentally measured cross-sectional shapes indicates that the assumed set of slip systems indeed activates. Note that these computations are independent of the strain hardening behavior.

In uniaxial compression of <111> oriented micropillars, there are 6 slip systems with identical Schmid factor (SF) and 6 slip systems with zero SF. From these 6 possibly active systems with non-zero SF, 3 systems develop strong collinear interactions with the forest dislocations in the other 3 systems. This prevents plastic flow from developing in 3 slip systems [20, 21]. Under these conditions, there are two distinct dispositions for the 3 active systems that produce stable uniaxial straining. One disposition involves development of glissile, coplanar and Lomer-Cottrell dislocation interactions [22], where the computed cross-section exhibits the quasi-elliptical appearance in Fig. 3(a). The second disposition in Fig. 3(b) exhibits 3 glissile interactions [22], where the cross-section retains its circular shape. Experimental assessment of the cross-sectional shape from the top surface of compressed micropillars along with EBSD measurements unambiguously show that all <111> oriented microcrystals develop the aforementioned quasi-elliptical shape (Fig. 4). This is direct evidence that plastic flow occurs under the activation of the 3 slip systems in Fig. 3(a).

Figs. 3(c)—(f) show the slip system dispositions for stable uniaxial straining along the <001> direction, where 4 slip systems activate from the 8 possible ones with the same SF [20, 33]. Again, this is because the strong collinear interaction prevents dislocation gliding in 4 of the equivalent systems. In this case, different cross-sectional shapes are found in the micropillar compression experiments, so that it is not possible to advocate development of one configuration in detriment of the others.

4.3. Mean-field modeling of the stress—strain curves in strain-hardening micropillars

This section describes strategies for the computation of the stress—strain curves in strain-hardening micropillars using the mean-field background in Section 3.1 in conjunction with the determined set of active slip systems in Section 4.2. While these

strategies provide unique stress—strain curves in <111> oriented micropillars, somewhat different curves are obtained for <001> micropillars depending on the sets of slip systems that activate in the experiments (Section 4.2). The latter results are not therefore given here for the sake of brevity.

Generalized plastic flow at $\tau > \tau_c$ involves further entanglement of the dislocation network that developed during the incipient plasticity stage. Two distinct scenarios for dislocation multiplication within this stage are considered here. In the case of <111> micropillars, dislocation configuration C_1 emerges through truncated source activation in the 3 active slip systems. All remaining inactive systems are dislocation free because for the value of $\rho^{\beta} = 1 \times 10^{10}$ m^{-2} in well annealed crystals, less than 1 dislocation per slip system becomes statistically available for $D < 10$ μm. The 6 inactive systems with vanishing SF do not contribute to strain hardening while little dislocation accumulation occurs in the 3 inactive systems with non-vanishing SF. For this dislocation configuration, application of Eq. (3) in micropillars with $D = 2$ μm renders the dislocation densities in Table 2(A) for the experimentally measured value of $\tau_o \approx 46$ MPa [for a total of ≈ 470 dislocation segments]. Dislocation storage (Eq. (5)) then yields the dislocation density ρ and junction density ρ_{jct} emerging in all slip systems at the experimentally measured value of $\tau_c = 64$ MPa (Table 2(A)); for a total of ≈ 1160 dislocation segments within the pillar. Fig. 5 finally shows the computed stress—strain curve at $\tau > \tau_c$ ($D = 2$ μm) while Table 2(A) provides all dislocation densities at $\varepsilon = 0.04$. Similar analyses are repeated for different micropillar diameters.

The second dislocation configuration C_2 under consideration accounts for experimental measurements in prestrained micropillars containing much greater dislocation densities than the bulk (parent) crystal prior to deformation [34, 35]. A prestrained micropillar

with $D = 2$ μm can be taken to exhibit $\rho^{\beta} \approx 1 \times 10^{13}$ m^{-2} (e.g., [36]) so that a total of ≈ 380 dislocation segments would become available if the dislocations were homogeneously distributed, rendering $\tau_c \approx 45$ MPa (Table 2(A)). Network development through junction formation would then result in the dislocation densities reported in Table 2(B) if τ_c was to occur at the same level of 64 MPa as in the above fresh micropillars [for a total of ≈ 450 dislocation segments]. Fig. 5 finally shows the computed stress—strain curve at $\tau > \tau_c$ while Table 2(B) provides all dislocation densities at $\varepsilon = 0.04$.

Given the present experimental variability (Fig. 1(a)), the good agreement between the stress—strain curves from experiments and simulations at various micropillar diameters is illustrated in Fig. 6 (configuration C_1). As described in Appendix A1, this can be further improved by accounting for dislocation cross-slip (see $y = 0.5$ nm in Fig. 5). It is also noted that configuration C_2 yields more prominent hardening than C_1.

The above results indicate that the concept of spatially uniform dislocation densities – underlying present continuum mechanics framework– applies to strain-hardening micropillars. Moreover, the finite element (FE) simulations (Appendix A2) performed with the current description capture the rather continuous flow patterns and the micropillar tilting behavior measured experimentally (Fig. 7). The FE simulations in Appendix A2 shed further light into the stability of uniaxial straining during testing.

4.4. Comparison between dislocation densities from experiments and simulations

The following discusses experimental evidence of dislocation storage from the literature in light of present strain hardening predictions. Transmission electron microscopy (TEM) analyses of (269)-oriented nickel micropillars with $D \gtrsim 10$ μm confirm development of dislocation patterning and storage, where the braid dislocation structure

resembles that attaining in a bulk [36]. Activation of three slip systems with different SF values is asserted in that work depending on the applied stress. The experimentally measured preexisting total density, ρ_T, $= \sum_{\beta=1}^{12} \rho^{\beta} = 6.5 \times 10^{12}$ m^{-2} suggests onset of incipient plasticity at $\sigma = 21$ MPa (Eq. (3)), approximating to the stress level that marks departure from linear elasticity for $D = 20$ μm. Generalized plastic flow is then experimentally detected at $\sigma \approx 35$ MPa. The initial dislocation density is found to increase during straining towards the maximum value of $\rho_T = 3.3 \times 10^{13}$ m^{-2} when D is in the range of 10 to 20 μm, which approximates to the presently predicted $\rho_T = 3.5 \times 10^{13}$ m^{-2} under bulk dislocation storage at the applied stress of $\sigma \approx 50$ MPa where the experiment is terminated ($D = 20$ μm). Since the dislocation junction arrangement provides milder strengthening than for the present (001), (011) and (111) orientations, $L_{eff} \approx 5$ μm is predicted at the onset of generalized flow ($\sigma \approx 35$ MPa at $D = 20$ μm). Consequently, $D/L_{eff} \rightarrow 4$ so that strain hardening dominates plastic flow (Section 5.1) in consonance with the rather smooth appearance of the stress—strain curve.

Further experimental evidence of dislocation storage during incipient plasticity is provided in [18] and [36], where marked surface dislocation annihilations preclude network development in micropillars that exhibit large plastic intermittencies (i.e., deforming within the confining plasticity regime described in Section 5.1). The experiments in [36] show that for $D = 1$ μm, generalized yielding occurs for $\sigma = 310$ MPa in 3 active slip systems with $\rho_T = 1.5 \times 10^{14}$ m^{-2}. While this value is significantly greater than the total density prior to straining ($\rho_T = 6.5 \times 10^{12}$ m^{-2}), it is still well below the presently predicted value of $\rho_T = 4 \times 10^{15}$ m^{-2}.

Dislocation density measurements in a (3-15)-oriented gold micropillar with $D = 0.8$ μm indicate dislocation accumulation in a single slip system with a small SF while the dislocations annihilate at the pillar surface in the two most favorably oriented systems [18]. The stress—strain curve also exhibits marked plastic intermittencies characteristic of the confining plasticity regime (Section 5.1). While for $\sigma = 240$ MPa measured ρ_T increased from the initial value of 1.7×10^{12} m^{-2} to 6.2×10^{12} m^{-2}, our computations show that it is not possible to accumulate a sufficient density so that the above applied stress level is reached with a single active slip system. The micropillars with $D = 6.3$ μm in [18] also display an increase in density during straining to $\rho_T = 2.5 \times 10^{12}$ m^{-2} ($\sigma = 48$ MPa), which is again much smaller than the value of $\rho_T = 8.3 \times 10^{13}$ m^{-2} anticipated within the present modeling scheme.

4.5. Dislocation avalanche statistics

Stress-integrated complementary cumulative distributions $C(s)_{\text{int}}$ are computed from present measurements of avalanche slips. Constant-stress slip s_σ and avalanche slip s_ε distributions and given in Figs. 8(a) and (b), respectively. Each distribution concerns 5 micropillar compression experiments (containing 200 slips s_σ and 400 slips s_ε) for the selected combinations of micropillar diameters and orientations in Fig. 1. The distributions are then fitted to Eq. (12) as described in Appendix A3.

5. Onset of the microscale plasticity regimes and associated dislocation avalanche statistics

5.1 Transition between strain hardening and confining plasticity

Directing attention to Fig. 6, microcrystals with D = 20 μm compressed along the <111> orientation exhibit the same stress—strain curve as that predicted through the

present strain hardening model in well-annealed bulk single-crystals (which deform from an initial low value of $\rho^{\beta} \approx 1 \times 10^{11}$ m^{-2} in all slip systems). For $D \lesssim 10$ μm, junction formation in extremely dense dislocation networks dominates plastic flow as described in Section 4.3. This leads to the onset of a microscale strain-hardening regime, where plastic deformations satisfy the same laws dictating dislocation storage in a bulk (Eq. (5)). It therefore becomes apparent that it is the vast dislocation density present in the active systems that ensures effective coarse graining of intermittency under the hypothesis of continuous flow for $D > 1$ μm. Hence, the small-scale behavior at large dislocation densities follows the same principles as bulk plasticity, where dislocation annihilations at the surfaces are largely inconsequential. It also stems from our results that the hypothesis of an unlimited supply of mobile dislocations from the bulk underlying Eq. (5) is fulfilled within the microscale strain hardening regime.

With further decreasing pillar size ($D \rightarrow 1$ μm), an increasing number of <111> microcrystals exhibit irregular or vanishing hardening ($\theta \rightarrow 0$), see Fig. 1(b) for $\tau > \tau_c$. This behavior denotes onset of a confining plasticity regime, where surface dislocation annihilations induce a stagnant dislocation network. The pillars are then found to exhibit marked slip traces at the surface (inset to Fig. 1(b)) that challenge the hypothesis of continuous flow. Whereas the shape of the stress—strain curves from these micropillars could be consistent with the attainment of source exhaustion hardening in the absence of dislocation storage, the results analyzed in Section 4.4 indicate that net storage indeed occurs within the incipient plasticity stage.

Section 4.4 further illustrates that the plastic intermittencies developing within the confining plasticity regime are triggered at greater shear stress levels than those associated with the onset of yielding under bulk strain hardening. The current mean-

field strain-hardening model cannot be therefore used to predict plastic flow within the confining plasticity regime, where limited dislocation storage always occurs. The effective shear stress resulting in truncated source operation thus equals the flow stress within the confining plasticity regime, which essentially varies depending of the availability of dislocation sources pivoting at a given distance from the sample surface.

In the transition between microscale strain-hardening and confining (exhaustion hardening) plasticity regimes, it is recognized that the pinning action of dislocation junctions is reduced with decreasing D [37]. The strengthening capacity of any given junction configuration could then be assessed by ratio D/L_{eff}, which measures the number of locations where a dislocation sweeping across the pillar becomes immobile as it interacts with the dislocation forest. Transition from strain hardening to confining plasticity is thus taken to occur as this ratio decreases below a critical level.

Our results for <001> and <111> micropillars show that $D/L_{eff} \gtrsim 2$ characterizes onset of the strain-hardening domain, whereas confining plasticity attains for $D/L_{eff} \lesssim 1.5$. It is noted that some <001> micropillars with D = 2 μm deforming within the strain-hardening regime exhibit sudden stress valleys passed some plastic strain level. This is attributed to statistical fluctuations in junction density, occurring in the proximity of $D/L_{eff} = 2$. Confining plasticity always prevails in micropillars with the <012> orientation (D < 10 μm), where D/L_{eff} remains below 1.5 because of mild dislocation storage in the two active slip systems. Along these lines, it is also noted that since the dislocation forest arising for the (269)-oriented micropillars in [36] (Section 4.4) is milder ($L_{eff} \approx 5$ μm) than that for the present (111)-oriented micropillars ($L_{eff} \approx 1$ μm), the microscale strain hardening domain is triggered at substantially greater values of D in the former where $D/L_{eff} > 2$ always prevails.

Ratio D/L_{eff} therefore becomes a fundamental dimensionless index describing transition in microscale plasticity regimes. Since L_{eff} is a function of loading orientation and dislocation density, index D/L_{eff} would be pertinent in investigating plastic flow in micropillars manufactured from prestrained crystals that contain an entangled preexisting dislocation network. Since L_{eff} is reduced for these micropillars, onset of strain-hardening at $D/L_{eff} > 2$ is favored for smaller diameters.

5.2. Emergence of self-organized criticality

The present experiments provide access to plastic intermittencies occurring in the active slip systems of crystals loaded in stress and strain control. As shown in Figs. 9 and 10, cumulative distribution functions $C(s_\varepsilon)$ and $C(s_\sigma)$ are not binned by stress while, in a similar vein, the mean avalanche slips from the raw data in Appendix A3 are stress-independent. These are key results furnishing experimental evidence in that the criticality level of the crystal remains constant during plastic straining irrespectively of the applied shear stress level. In the context of Eq. (11), difference $(\tau^* - \tau)$ can then be taken to remain constant, so that any increase in applied stress τ due to strain hardening is counterbalanced by a raise in criticality stress τ^*. This is the first convincing experimental evidence in that self-organized criticality (SOC) rather than stress-tuned criticality (STC) rules dislocation avalanching processes in micrometer-sized crystals. Moreover, since the slip distributions of micropillars deforming within the confining and strain-hardening plasticity regimes are not stress binned (Figs. 9 and 10), SOC becomes a general paradigm in micrometer-sized samples.

Following Fig. 8, measured avalanche size distributions are accurately fitted through Eq. (11). In the transition from confining to strain-hardening plasticity, the values of $s_{\max}$ obtained from the above fit decrease from $\approx 17b$ to $7b$ for s_ε counts ($\gamma_{\max} \approx 1.2 \times$

10^{-3} and 3.0×10^{-4}, respectively) and from $s_{\max} \approx 55b$ to $13b$ for s_σ counts ($\gamma_{\max} \approx 3.9 \times 10^{-3}$ and 5.5×10^{-4}, respectively). It is further noticed that present $C(s_\varepsilon)_{\text{int}}$ and $C(s_\sigma)_{\text{int}}$ functions defy the STC scaling of $\sim s^{-1}$ (Section 3.2). These functions thus exhibit a gradual cut-off for $s \to s_{\max}$ that is more in accordance with Eq. (11).

5.3. Dislocation storage and the transition from self-organized to stress-tuned criticality

The above results represent convincing evidence in that it is the entanglement of the dislocation network occurring at the incipient plasticity stage that governs the slip distribution of dislocation avalanches. The development of heavily entangled dislocation networks thus reduces the size of dislocation avalanches through junction zipping and unzipping processes, so that the slip distributions become a fingerprint of the active plasticity regime (Fig. 8). This contradicts the mild influence of strain hardening upon the value of $s_{\max}$ predicted in [15] (Section 3.2).

The above fundamental interpretation holds irrespectively of the effect of pillar size upon the magnitude $\Delta\sigma$ of a stress serration (Eq. (2)). It is noticed that since $\Delta\sigma = s_\varepsilon \times E \times SF/l$, the stress serrations would exhibit a two-fold increase with a two-fold decrease in pillar length l. Nevertheless, as confining plasticity sets-in, our experiments show that a *four-fold increase* in $\Delta\sigma$ attains with such a two-fold decrease in l. Secondly, whereas an increase in $s_{\max}$ would be theoretically predicted to arise with increasing pillar size (Section 3.2), a *reduction* in $s_{\max}$ marks the current transition towards strain hardening plasticity with increasing pillar sizes (Fig. (8)).

Measured slip distributions indicate that while the number of dislocations N contained in an avalanche increases for large values of the mean free path L_{eff}, this is only so when there is a shift from the confining to the microscale strain hardenings domains.

The crystal therefore emits a larger number of dislocations when the arresting locations along the active slip plane decrease below a critical number. This is rationalized in that

$$s_{\max} \sim f_{\varepsilon,\sigma}(D/L_{eff}) \quad , \tag{14}$$

where functions $f_{\varepsilon,\sigma}$ exhibit sudden variations in the transition from strain hardening to confining plasticity. Function f_{ε} for s_{ε} counts varies from 1.0 to ≈ 2.5 while function f_{σ} for s_{σ} counts varies from 1.0 to ≈ 4.2. Within the present range of micropillar sizes, our results also indicate that $f_{\varepsilon,\sigma}$ remain roughly constant up to $D/L_{eff} = 6$.

The present findings unravel the statistical features of dislocation avalanches in crystal plasticity. In this sense, recent experimental results have demonstrated that plasticity in submicrometer-sized crystals adheres to the principle of STC, where the crystal responds with greater avalanches when the applied stress approaches τ^* [16]. By contrast, in the present crystals with characteristic dimension $D \gtrsim 1$ μm, SOC rules dislocation avalanches in both strain hardening and confining plasticity regimes. This is an outcome of dislocation storage processes arising within the incipient plasticity stage of micrometer-sized crystals, which are suppressed in submicrometer sizes. Since SOC unfolds even for the less entangled networks developing along the <012> orientation, this paradigm would prevail in bulk samples with smaller dislocation densities.

6. Concluding remarks

1. The development of a dense dislocation network during an incipient plasticity stage characterizes plastic flow in micrometer-sized samples. We show that the combined role of sample size, loading orientation and dislocation density upon the onset of strain hardening can be assessed through a mean-field dimensionless index. Microscale strain hardening plasticity thus emerges when the ratio between the characteristic sample size and the mean free path travelled by the mobile

dislocations, D/L_{eff}, > 2. Under this condition, the strengthening capacity of the dislocation network is sufficient as to ensure that plastic flow involves dislocation storage irrespectively of dislocation annihilation processes at the sample surface. The domain of confining plasticity distinguished by insufficient network development then attains for $D/L_{eff} < 1.5$. Plastic straining in this regime is characterized by vanishing hardening under a stagnant dislocation network. As opposed to plasticity in submicrometer dimensions where surface dislocation annihilations may result in dislocation-starved samples, dislocation storage is thus the distinctive feature underlying plasticity in micrometer-sized samples.

2. The statistical description of dislocation avalanches in micrometer-sized crystals is in accordance with the paradigm of self-organized criticality (SOC), where the size of such plastic intermittencies is a function of the strain hardening behavior irrespectively of the applied stress level. There is therefore a fundamental distinction between the dislocation avalanche statistics that apply to samples with micrometer and submicrometer sizes, as criticality is tuned by stress in the latter. Our results are all consistent in that the inception of a dislocation network under multiple-glide is the essential feature leading to SOC.
3. The size of the dislocation avalanches is reduced under the highly entangled dislocation networks characterizing microscale strain-hardening plasticity. This is a direct consequence of junction zipping processes between the mobile dislocations in the avalanche and the forest dislocations in the interacting slip systems at $D/L_{eff} > 2$. Conversely, it is found that the strengthening provided by such junction forming processes is strongly diminished within the domain of confining plasticity. Severe plastic intermittencies consequently develop for $D/L_{eff} < 1.5$.

4. Continuum crystal plasticity is instrumental in the modeling of strain hardening at the microscale. The key parameters governing plastic flow are the forest dislocation density ρ^{β} in Eq. (3) and the mean free path traveled by the mobile dislocations L_{eff} from the dislocation storage law in Eq. (5). The dislocation density thus becomes the scaling parameter that enables computation of the stress—strain curves at the vast dislocation densities developing in microcrystalline samples. With decreasing dislocation density, present microscale strain-hardening domain naturally converges into bulk plasticity where smaller flow stresses prevail. The excellent agreement between the stress—strain curves from experiments and mean-field simulations further indicates that while dislocation annihilations inevitably occur at the surface, this phenomenon can be largely ignored under microscale strain hardening.
5. The framework of continuum crystal plasticity has been used to evaluate slip system activity in micropillar compression experiments. The devised analytical procedure employs Eq. (9) from the text in conjunction with EBSD measurements of the plastic distortion in the top surface of compressed micropillars. It is demonstrated that the comparison between computed and experimentally measured plastic distortions provides direct evidence on the activity of specific sets of slip systems. These analyses are particularly useful in micropillars deforming under the microscale strain-hardening domain, where the assertion of slip system activity becomes difficult from the fainting slip traces at the sample surface.

Acknowledgements: The authors acknowledge insightful discussions with L. Kubin. Financial support was provided by Ministerio de Economía y Competitividad Grant MAT2011-23375 (Spain) and CENTEM projects CZ.1.05/2.1.00/03.0088 and PLUS LO1402 (Czech Republic).

References

1. J. Friedel, Dislocations, Pergamon, Oxford, 1964.

2. D. Kuhlmann-Wilsdorf, Metall. Trans. A **16A**, 2091 (1985).

3. U. F. Kocks, H. Mecking, Prog. Mater. Sci. **48**, 171 (2003).

4. H. Tang, K.W. Schwarz and H. D. Espinosa, Phys. Rev. Lett. **100**, 185503 (2008).

5. S. H. Oh, M. Legros, D. Kiener and G. Dehm, Nature Mat. **8**, 95 (2009).

6. J. R. Greer and W. D. Nix, Phys. Rev. B. **73**, 245410 (2006).

7. T.A. Parthasarathy, S.I. Rao, D-M. Dimiduk, M.D. Uchic, D.R. Trinle, Scripta Mater. **56**, 313 (2007).

8. J. A. El-Awady, S. I. Rao, C. Woodward, D. M. Dimiduk, M. D. Uchic, Int. J. Plasticity **27**, 372 (2011).

9. C. Zhou, I.J. Beyerlein, R. LeSar, Acta Mater. **59**, 7673 (2011)

10. A.A. Benzerga, Int. J. Plasticity **24**, 1128 (2008).

11. S.I. Rao, D.M. Dimiduk, T.A. Parthasarathy, M.D. Uchic, M. Tang, C. Woodward, Acta Mater. **56**, 3245 (2008).

12. C. Motz, D. Weygand, J. Senger. P. Gumbsch, Acta Mater. **57** 1744 (2009).

13. M.D. Uchic, P.A. Shade, D.M. Dimiduk, Annu. Rev. Mater. Res. **39** 361 (2009).

14. D.M. Dimiduk, C. Woodward, R. LeSar, M.D. Uchic, Science **312**, 1188 (2006).

15. F.F. Csikor, C. Motz, D. Weygand, M. Zaiser, S. Zapperi, Science **318**, 251 (2007).

16. N. Friedman, A. T. Jennings, G. Tsekenis, J-Y. Kim, M. Tao, J. T. Uhl, J. R. Greer and K. A. Dahmen, Phys. Rev. Lett., **109**, 095507 (2012).

17. K.A. Dahmen, Y. Ben-Zion, J.T. Uhl, Phys. Rev. Lett., **102**, 175501 (2009).

18. K.S. Ng and A.H.W. Ngan, Acta Mater. **56**, 1712 (2008).

19. D. Kiener, P.J. Guruprasad, S.M. Keralavarma, G. Dehm, A.A. Benzerga, Acta Mater. **59**, 3825 (2011).

20. B. Devincre, T. Hoc, L. Kubin. Science **320**, 1745 (2008).

21. L. Kubin, B. Devincre, T. Hoc, Acta Mater. **56**, 6040 (2008).

22. P. Franciosi, A. Zaoui, Acta Metall. **30**, 1627 (1982).

23. Basinski SJ, Basinski ZS. In: Nabarro FRN, editor. Dislocations in solids, Vol. 4. Amsterdam: North-Holland; 1979. p. 261.

24. R.J. Asaro, Adv. Appl. Mech. **23**, 1 (1983).

25. M.-C. Miguel, A. Vespignani, S. Zapperi, J. Weiss, J.-R. Grasso, Mater. Sci. Engng. A, **309–310**, 324 (2001).

26. P. Moretti, M.-C. Miguel, M. Zaiser, S. Zapperi, Phys. Rev. B **69**, 214103 (2004).

27. M. Zaiser, Adv. Phys. **55**, 185 (2006).

28. M. Zaiser and P. Moretti, J. Stat. Mech. P08004 (2005).

29. S. Papanikolaou, D.M. Dimiduk, W. Choi, J.P Sethna, M.D. Uchic, C.F. Woodward, S. Zapperi, Nature **490**, 517 (2012).

30. D. Markovic, C. Gros, Physics Reports **536**, 41 (2014).

31. M.C. Miguel, A. Vespignani, S. Zapperi, J. Weiss, J.R. Grasso, Nature **410**, 667 (2001).

32. S. Akarapu, H.M. Zhib, D.F. Bahr, Int. J. Plasticity **26**, 239 (2010).

33. R. Madec, B. Devincre, L. Kubin, T. Hoc, D. Rodney, Science **301**, 1879 (2003).

34. S-W. Lee, S. M. Han, W.D. Nix, Acta Mater **57**, 4404 (2009).

35. J. A. El-Awady, M. D. Uchic, P. A. Shade, S.-L. Kim, S. I. Rai, D. M. Dimiduk, C. Woodward, Scr. Mater. **68**, 207 (2013).

36. D.M. Norfleet, D.M. Dimiduk, S.J. Polasika, M.D. Uchic, M.J. Mills, Acta Mater. **56**, 2988 (2008).

37. J. G. Sevillano, I.O. Arizcorreta, L.P. Kubin, Mater Sci. Eng. A **309**, 393 (2001).

Table 1: Dislocation interaction and storage parameters for fcc crystals

b (Å)	μ (GPa)	p_0	k_0	κ_0	y (nm)	K_0	K_c	$a_{\text{self, ref}}$	$a_{\text{collinear, ref}}$	$a_{\text{Hirth, ref}}$	$a_{\text{coplanar, ref}}$	$a_{\text{glissile, ref}}$	$a_{\text{Lomer, ref}}$	ρ_{ref} (m^{-2})	n
2.56 [a]	42 [a]	0.117	1.08	0.225	50 [a]	180	180	0.112	0.625	0.070	0.122	0.125	0.122	10^{12}	$4^{\dagger}; 3^{\ddagger}; 2^{\S}$

†,‡,§ for uniaxial pulling along the <001>, <111> and <012>, respectively

Subscripts self, ref; collinear, ref; Hirth, ref; coplanar, ref; glissile, ref; and Lomer, ref concern dislocation interactions resulting from the specific $\alpha\beta$ slip system combinations in [22] measured at the reference dislocation density of 1×10^{12} m^{-2}.

[a] for pure copper.

Table 2A: Dislocation configuration C_1 for (111) micropillars with D = 2 μm

Slip plane	Slip direction	τ_o (MPa)	ρ_o (m^{-2})	$\rho_{o,jct}$ (m^{-2})	τ_c (MPa)	ρ_c (m^{-2})	$\rho_{c,jct}$ (m^{-2})	L_{eff} (μm)	τ (MPa) @ ε = 4%	ρ (m^{-2}) @ ε = 4%	ρ_{jct} (m^{-2}) @ ε = 4%	L_{eff} (μm) @ ε = 4%
(1 1 1)	[0 -1 1]	-	$< 1 \times 10^{6}$	0	-	$< 1 \times 10^{6}$	4.94×10^{5}		-	$< 1 \times 10^{6}$	1.12×10^{6}	
(1 1 1)	[1 0 -1]	-	$< 1 \times 10^{6}$	0	-	$< 1 \times 10^{6}$	4.85×10^{5}		-	$< 1 \times 10^{6}$	1.09×10^{6}	
(1 1 1)	[-1 1 0]	-	$< 1 \times 10^{6}$	0	-	$< 1 \times 10^{6}$	4.82×10^{5}		-	$< 1 \times 10^{6}$	1.09×10^{6}	
(-1 1 1)	[1 0 1]	47	5×10^{13}	0	64	1.14×10^{14}	1.27×10^{13}	1.30	91	2.98×10^{14}	5.13×10^{13}	0.94
(-1 1 1)	[1 1 0]	46	5×10^{13}	0	64	1.12×10^{14}	1.22×10^{13}	1.30	90	2.93×10^{14}	4.92×10^{13}	0.94
(-1 1 1)	[0 -1 1]	-	$< 1 \times 10^{6}$	0	-	$< 1 \times 10^{6}$	1.36×10^{5}		-	$< 1 \times 10^{6}$	3.08×10^{5}	
(1 -1 1)	[0 1 1]	-	$< 1 \times 10^{6}$	0	-	$< 1 \times 10^{6}$	2.08×10^{5}		-	$< 1 \times 10^{6}$	4.64×10^{5}	
(1 -1 1)	[1 1 0]	-	$< 1 \times 10^{6}$	0	-	$< 1 \times 10^{6}$	2.26×10^{5}		-	$< 1 \times 10^{6}$	5.14×10^{5}	
(1 -1 1)	[1 0 -1]	-	$< 1 \times 10^{6}$	0	-	$< 1 \times 10^{6}$	4.83×10^{5}		-	$< 1 \times 10^{6}$	1.09×10^{6}	
(1 1 -1)	[0 1 1]	47	5×10^{13}	0	64	1.44×10^{14}	2.95×10^{13}	0.97	90	3.75×10^{14}	1.22×10^{14}	0.75
(1 1 -1)	[1 0 1]	-	$< 1 \times 10^{6}$	0	-	$< 1 \times 10^{6}$	1.13×10^{5}		-	$< 1 \times 10^{6}$	2.58×10^{5}	
(1 1 -1)	[-1 1 0]	-	$< 1 \times 10^{6}$	0	-	$< 1 \times 10^{6}$	3.12×10^{5}		-	$< 1 \times 10^{6}$	7.04×10^{5}	

Grey rows indicate active systems

Table 2B: Dislocation configuration C_2 for (111) micropillars with D = 2 μm

Slip plane	Slip direction	τ_o (MPa)	ρ_o (m^{-2})	$\rho_{o,jct}$ (m^{-2})	τ_c (MPa)	ρ_c (m^{-2})	$\rho_{c,jct}$ (m^{-2})	L_{eff} (μm)	τ (MPa) @ ε = 4%	ρ (m^{-2}) @ ε = 4%	ρ_{jct} (m^{-2}) @ ε = 4%	L_{eff} (μm) @ ε = 4%
(1 1 1)	[0 -1 1]	-	1×10^{13}	0	-	1×10^{13}	4.02×10^{12}	-	-	1×10^{13}	9.99×10^{12}	
(1 1 1)	[1 0 -1]	-	1×10^{13}	0	-	1×10^{13}	3.86×10^{12}	-	-	1×10^{13}	9.59×10^{12}	
(1 1 1)	[-1 1 0]	-	1×10^{13}	0	-	1×10^{13}	3.93×10^{12}	-	-	1×10^{13}	9.71×10^{12}	
(-1 1 1)	[1 0 1]	45	1×10^{13}	0	64	7.65×10^{13}	5.72×10^{12}	1.10	93	2.89×10^{14}	3.95×10^{13}	0.80
(-1 1 1)	[1 1 0]	45	1×10^{13}	0	64	7.58×10^{13}	5.42×10^{12}	1.10	92	2.84×10^{14}	3.74×10^{13}	0.80
(-1 1 1)	[0 -1 1]	-	1×10^{13}	0	-	1×10^{13}	1.07×10^{12}	-	-	1×10^{13}	2.67×10^{13}	
(1 -1 1)	[0 1 1]	-	1×10^{13}	0	-	1×10^{13}	2.34×10^{12}	-	-	1×10^{13}	5.15×10^{13}	
(1 -1 1)	[1 1 0]	-	1×10^{13}	0	-	1×10^{13}	2.45×10^{12}	-	-	1×10^{13}	5.51×10^{12}	
(1 -1 1)	[1 0 -1]	-	1×10^{13}	0	-	1×10^{13}	3.96×10^{12}	-	-	1×10^{13}	9.74×10^{12}	
(1 1 -1)	[0 1 1]	45	1×10^{13}	0	64	8.67×10^{13}	1.20×10^{13}	0.92	92	3.51×10^{14}	8.88×10^{13}	0.64
(1 1 -1)	[1 0 1]	-	1×10^{13}	0	-	1×10^{13}	1.23×10^{12}	-	-	1×10^{13}	2.77×10^{12}	
(1 1 -1)	[-1 1 0]	-	1×10^{13}	0	-	1×10^{13}	2.52×10^{12}	-	-	1×10^{13}	6.23×10^{12}	

Grey rows indicate active systems

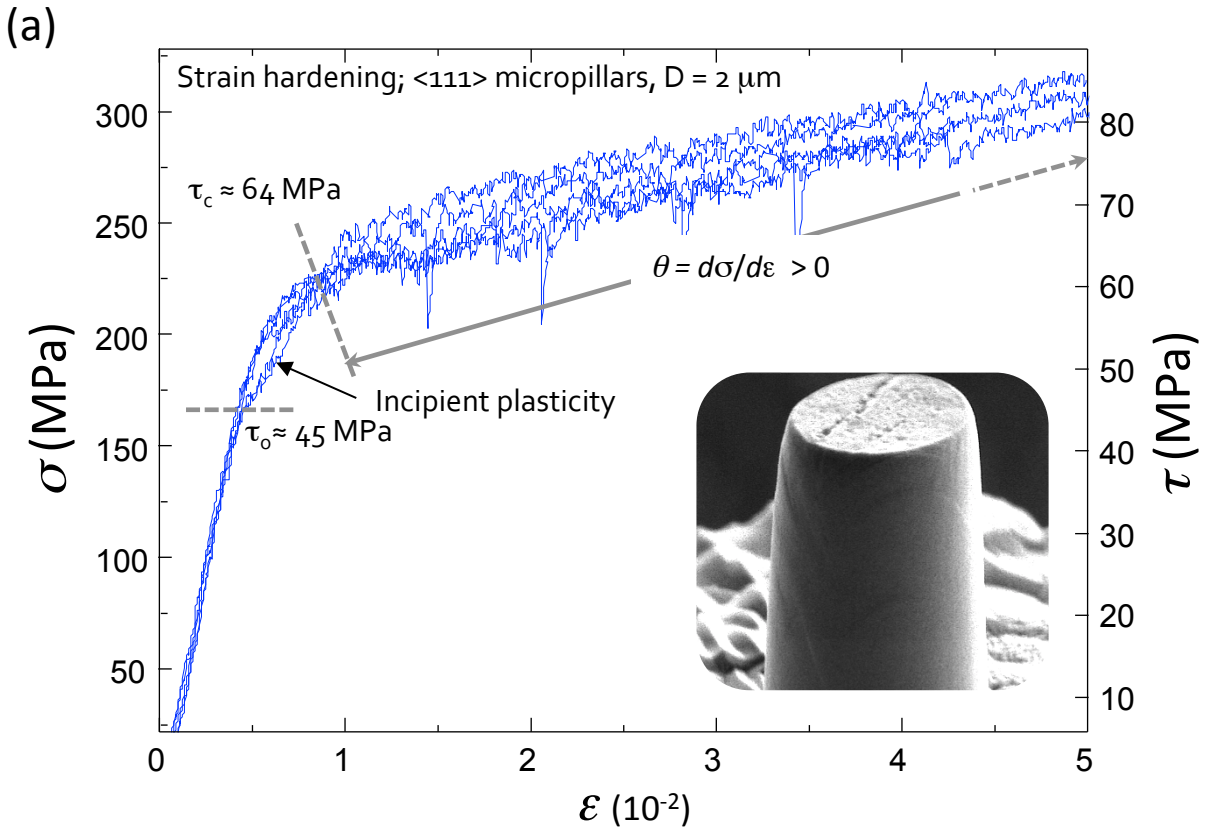

Fig. 1: Uniaxial stress (σ)—logarithmic strain (ε) curves for different micropillar diameters and orientations. (a) <111> micropillars deforming within the strain hardening domain. The inset shows rather continuous flow along the micropillar length with faint slip traces. (b) Confining plasticity where the insets show slip traces including dual glide deformation patterns for <012> micropillars. For all micropillar orientations in the figures, the stage of incipient plasticity attains at intermediate values from τ_o and τ_c.

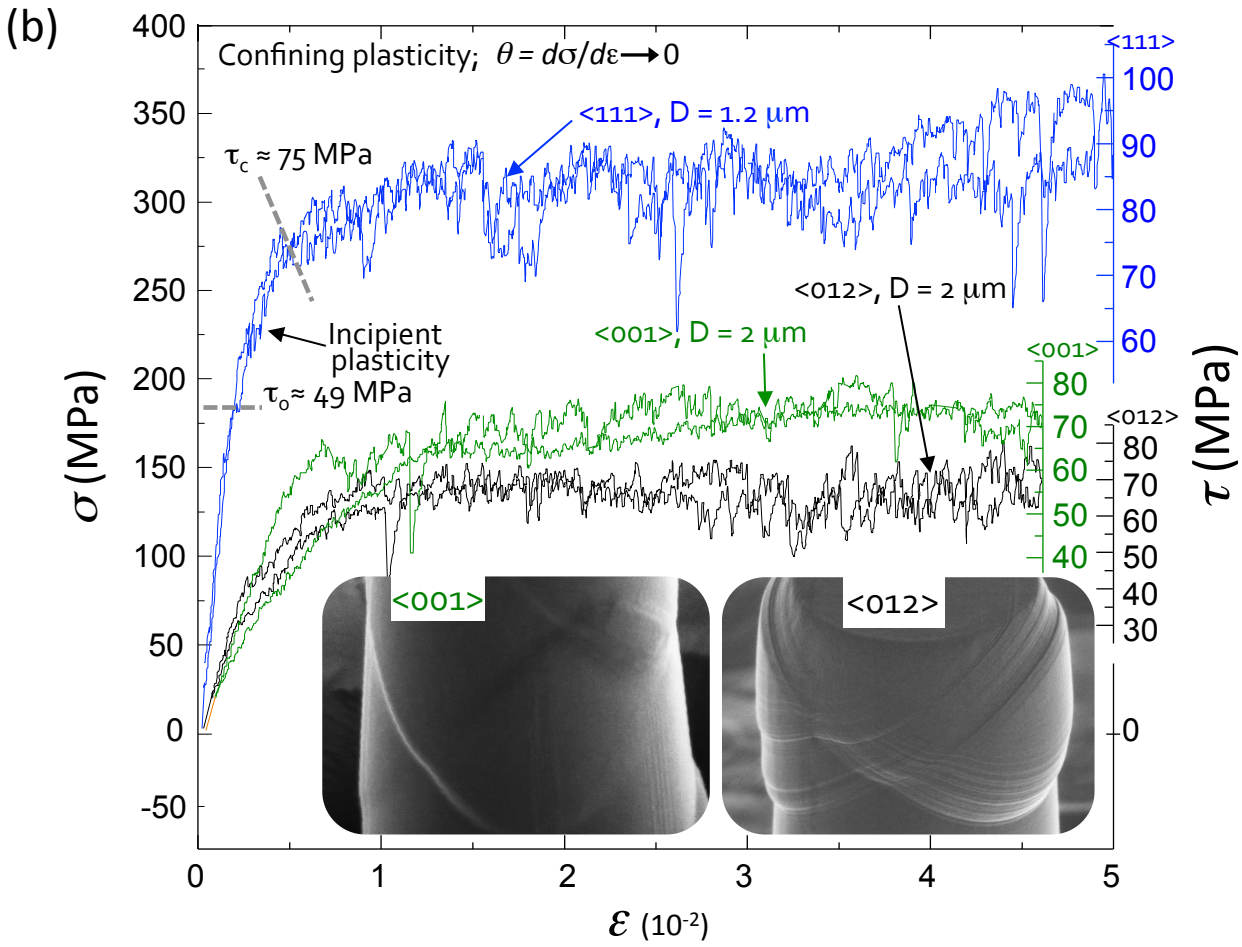

Fig. 1: Uniaxial stress (σ)—logarithmic strain (ε) curves for different micropillar diameters and orientations. (a) <111> micropillars deforming within the strain hardening domain. The inset shows rather continuous flow along the micropillar length with faint slip traces. (b) Confining plasticity where the insets show slip traces including dual glide deformation patterns for <012> micropillars. For all micropillar orientations in the figures, the stage of incipient plasticity attains at intermediate values from τ_o and τ_c.

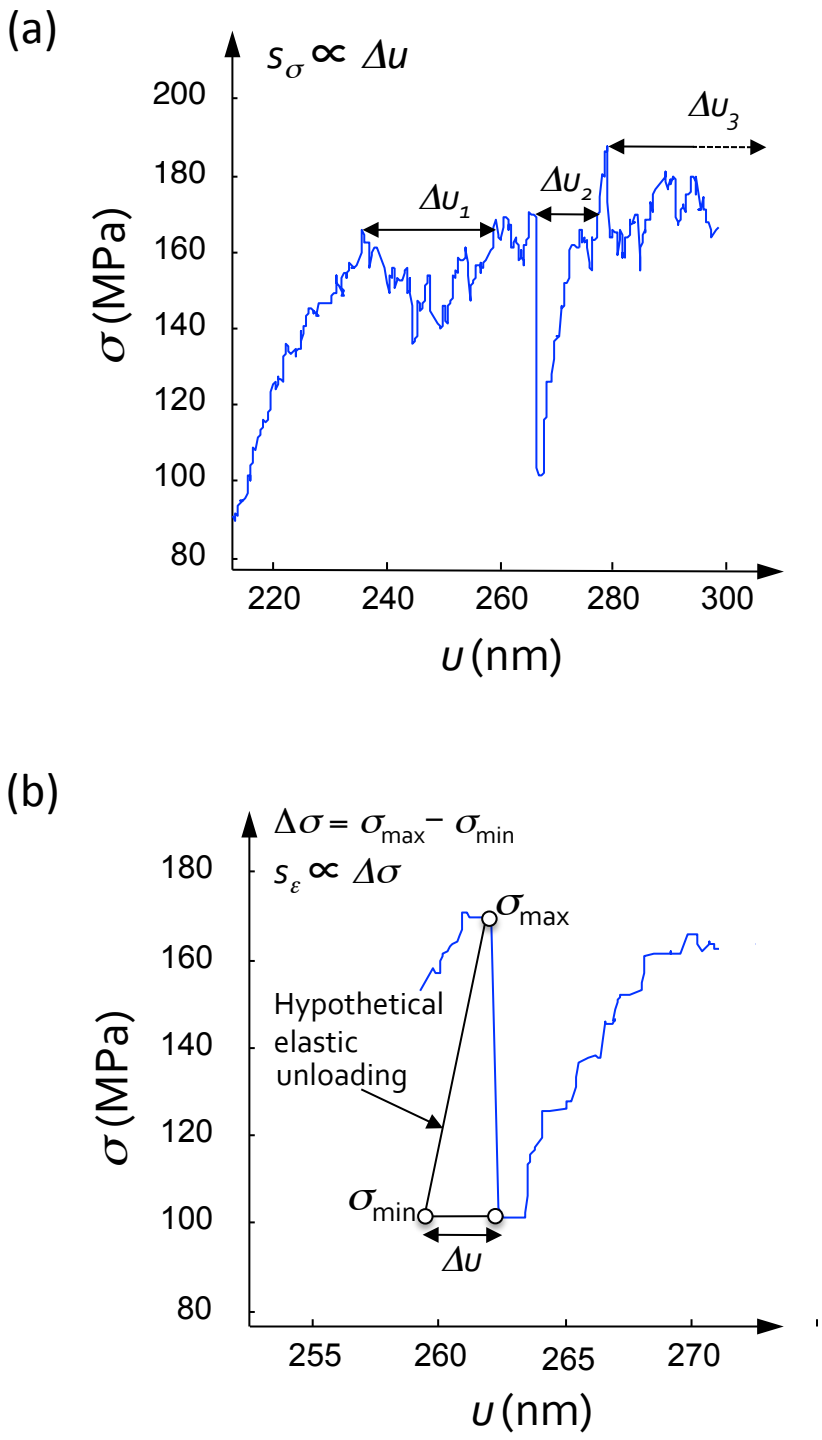

Fig. 2: Schematic of plastic intermittencies and associated nomenclature. (a) Constant load (or stress) slips due to plastic strain increments Δu. (b) Slip associated with an individual dislocation avalanche characterized by stress serration $\Delta\sigma$. Δu measures the difference between the instantaneous pillar length passed the avalanche and the length immediately before the onset of the avalanche. The latter is computed by assuming elastic unloading to σ_{min}, so that the micropillar is loaded to the same stress level prior and after the avalanche.

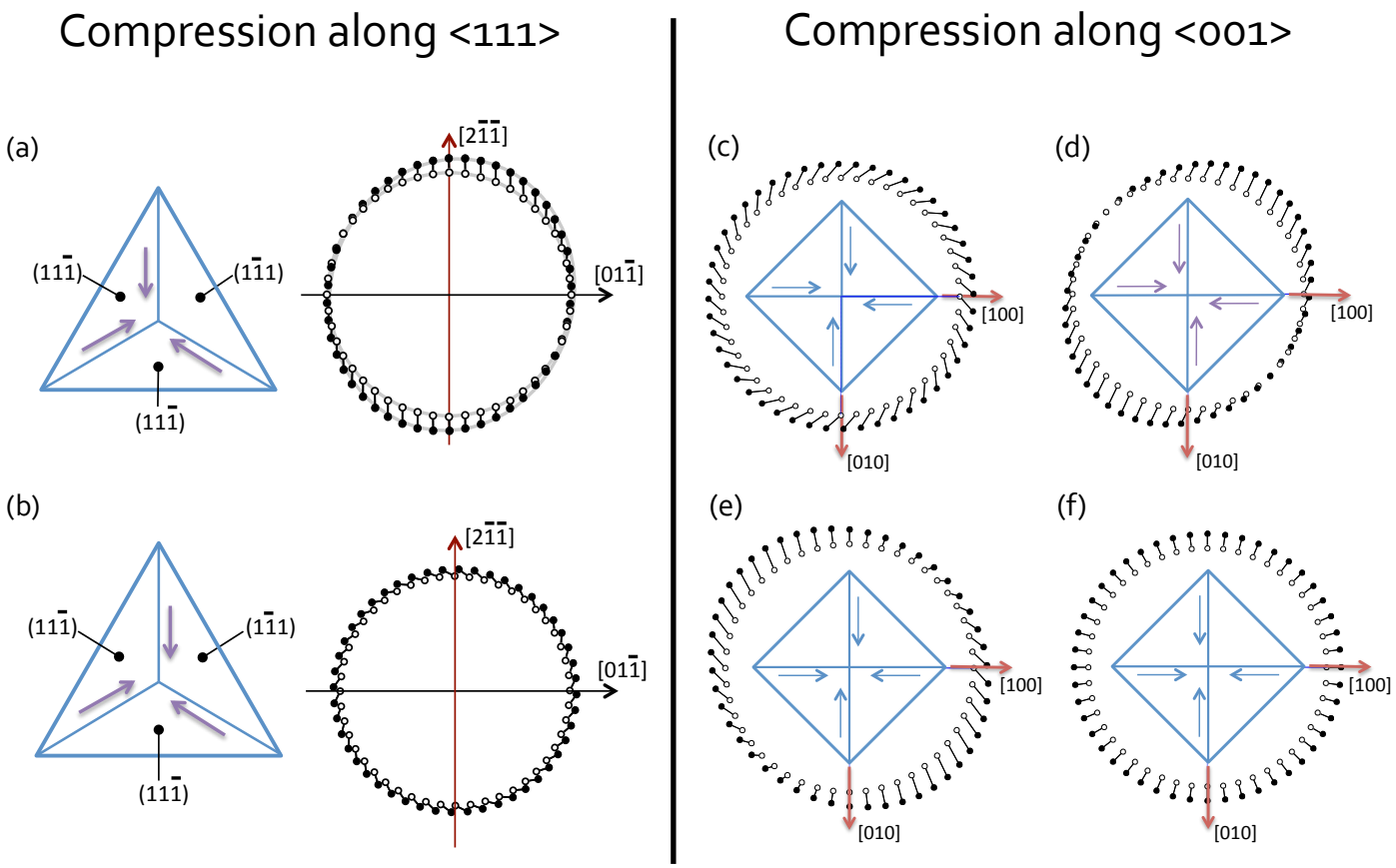

Fig. 3: Possible sets of active slip systems for uniaxial straining of <111> and <001> oriented micropillars. Parts (a) and (b) illustrate the two possible sets of active systems for <111> micropillars. Activation of each set of slip systems results in the cross sectional shapes depicted in the right hand side of Parts (a) and (b). Empty points are for the circular (undeformed) cross-section and filled points are for the deformed state. Parts (c)—(f) illustrate the four possible sets of active slips systems in <001> micropillars, where the empty points of the circular (undeformed) cross-sectional shape are again connected to the filled points in the deformed state.

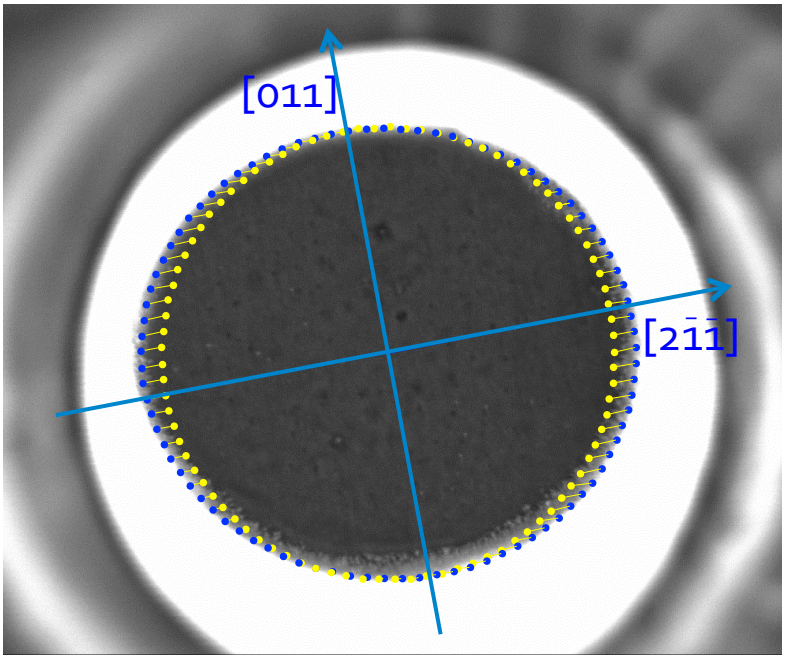

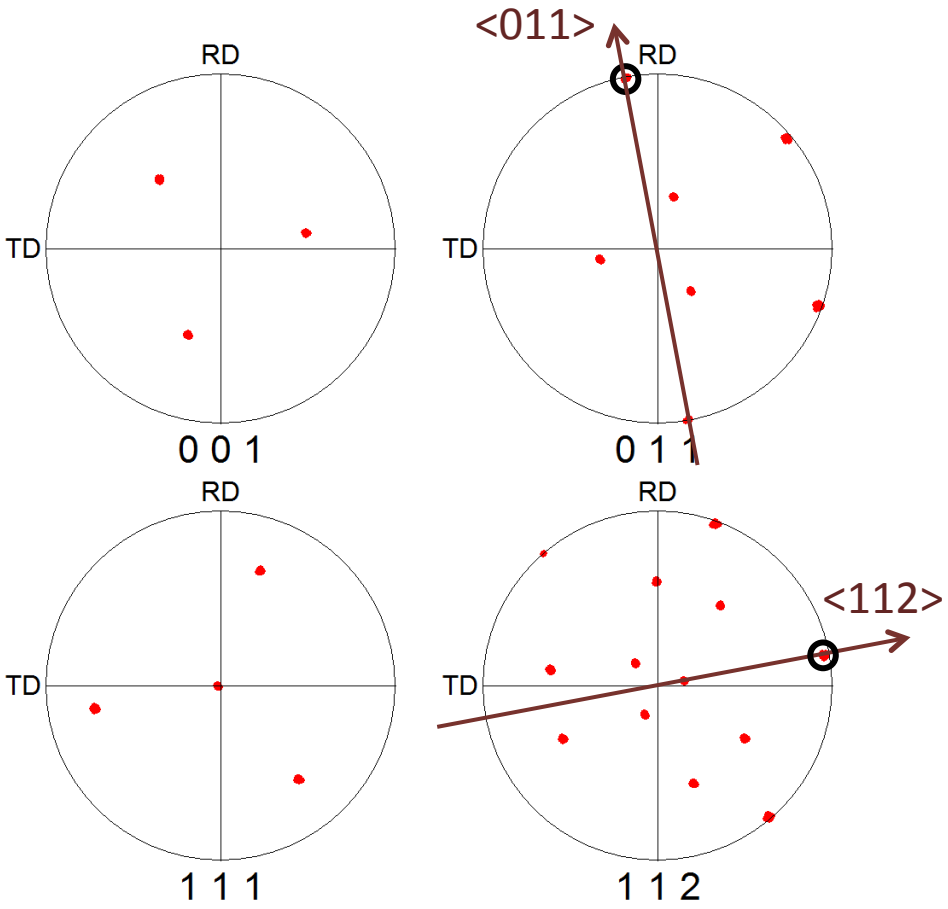

Fig. 4: Crystallographic analyses of the plastic distortion in the top surface of compressed <111> micropillars. The evolution of the circular (undeformed) cross-sectional shape to the deformed configuration computed for the set of slip systems in Fig. 3(a) at ε = 4% is given in the top figure. Notice that the crystallographic character of the computed plastic distortion matches actual measurements in the micropillar. Associated EBSD analyses are given in the bottom.

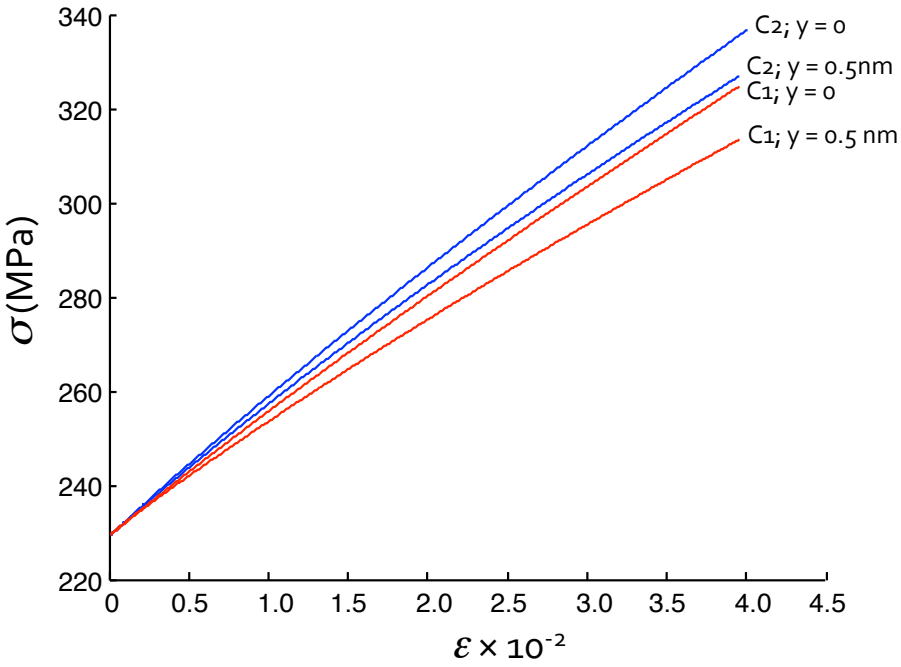

Fig. 5: Uniaxial stress (σ)—logarithmic strain (ε) curves computed for the strain-hardening <111> micropillars in Fig. 1(a). Two dislocation configurations termed C_1 and C_2 are assumed in the computations. Configuration C_1 concerns a dislocation network emerging in the three active slips systems. Configuration C_2 concerns a micropillar with a preexisting dense dislocation arrangement. Parameter y = 0 is for dislocation storage without cross-slip and y = 0.5 nm accounts for dislocation cross-sip in pure copper. See text and Appendix A2 for details.

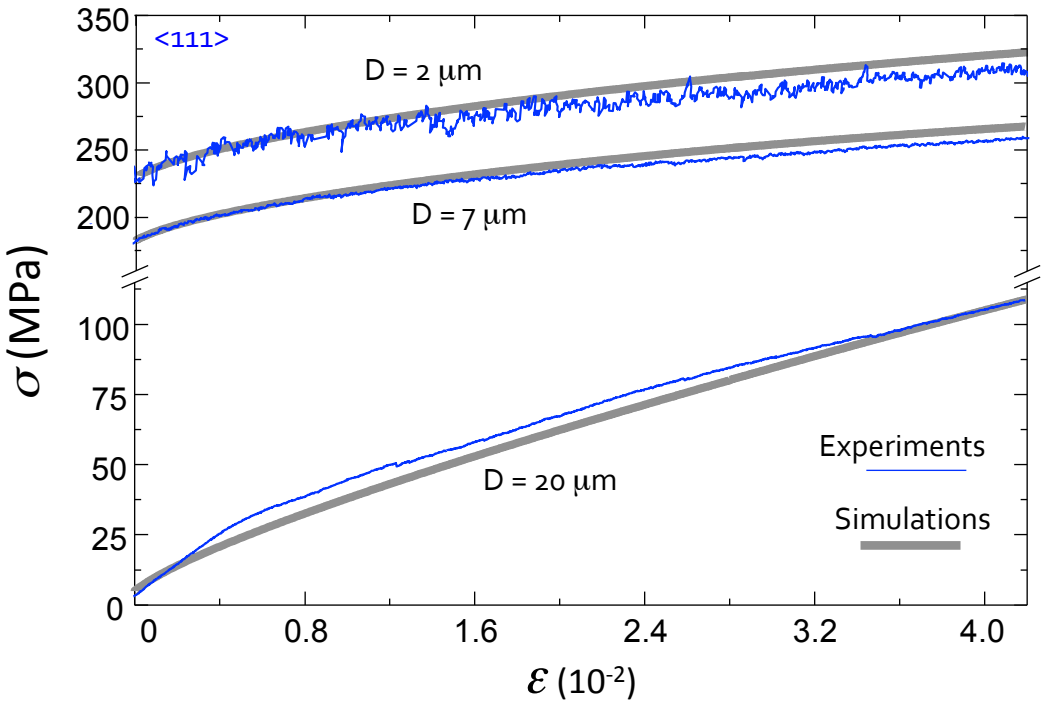

Fig. 6: Representative uniaxial stress (σ)—logarithmic strain (ε) curves from experiments and simulations for strain-hardening <111> oriented micropillars with different diameters. (Experimental variability is illustrated in Fig. 1(a).) The simulations are for dislocation configuration C_1 in the absence of dislocation cross-slip (y = 0). Accounting for cross-slip further improves agreement between experiments and simulations.

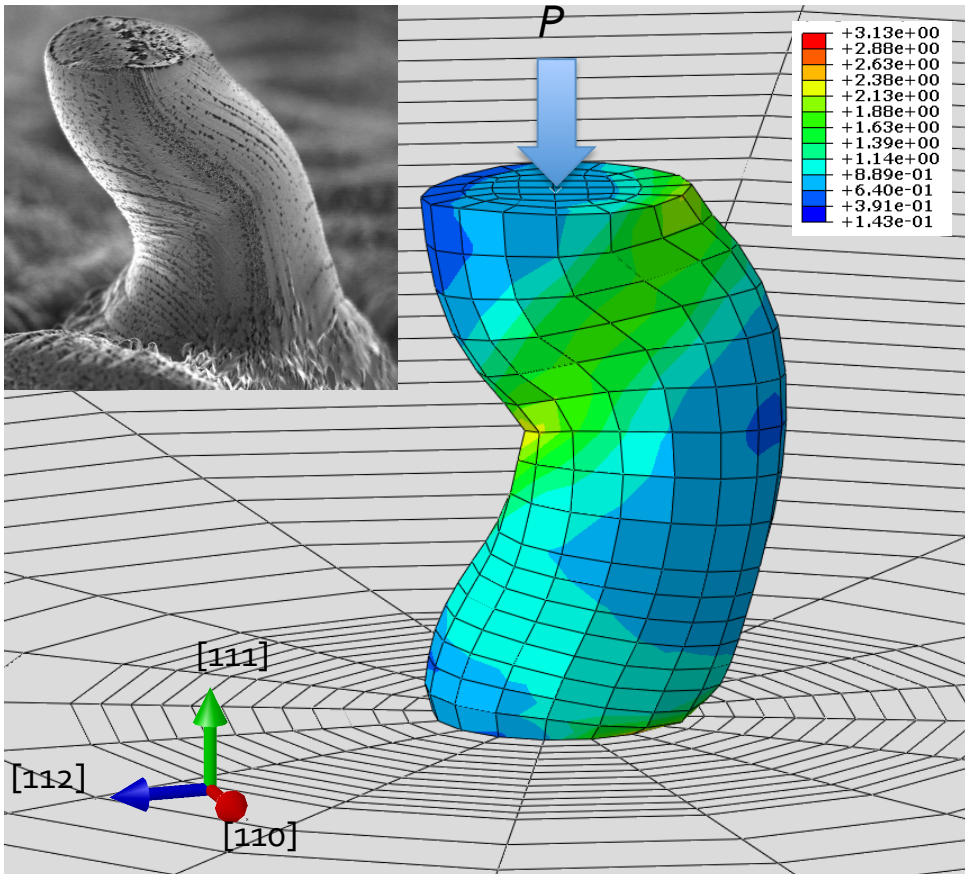

Fig. 7: Rather continuous flow in experiments with strain-hardening <111> oriented micropillars and comparison with finite element (FE) simulations. The results are for D = 7 μm at ε = 0.3. In the FE simulation, the isocontours are of the total shear strain in all slip systems.

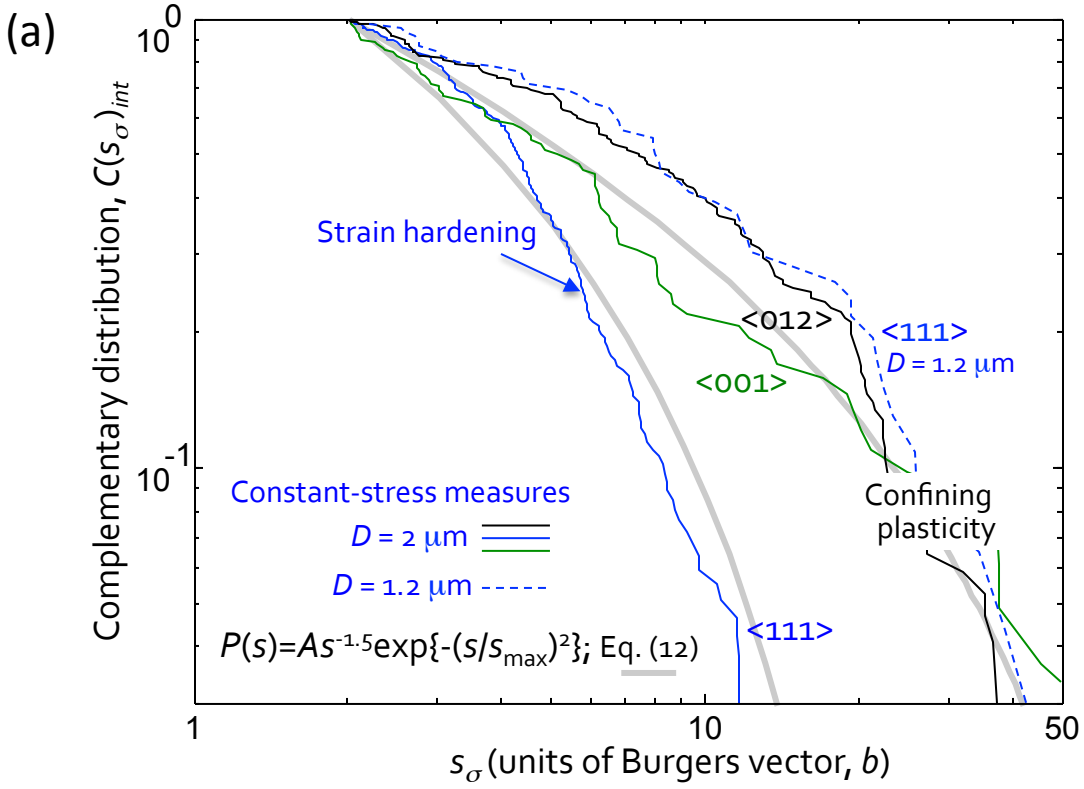

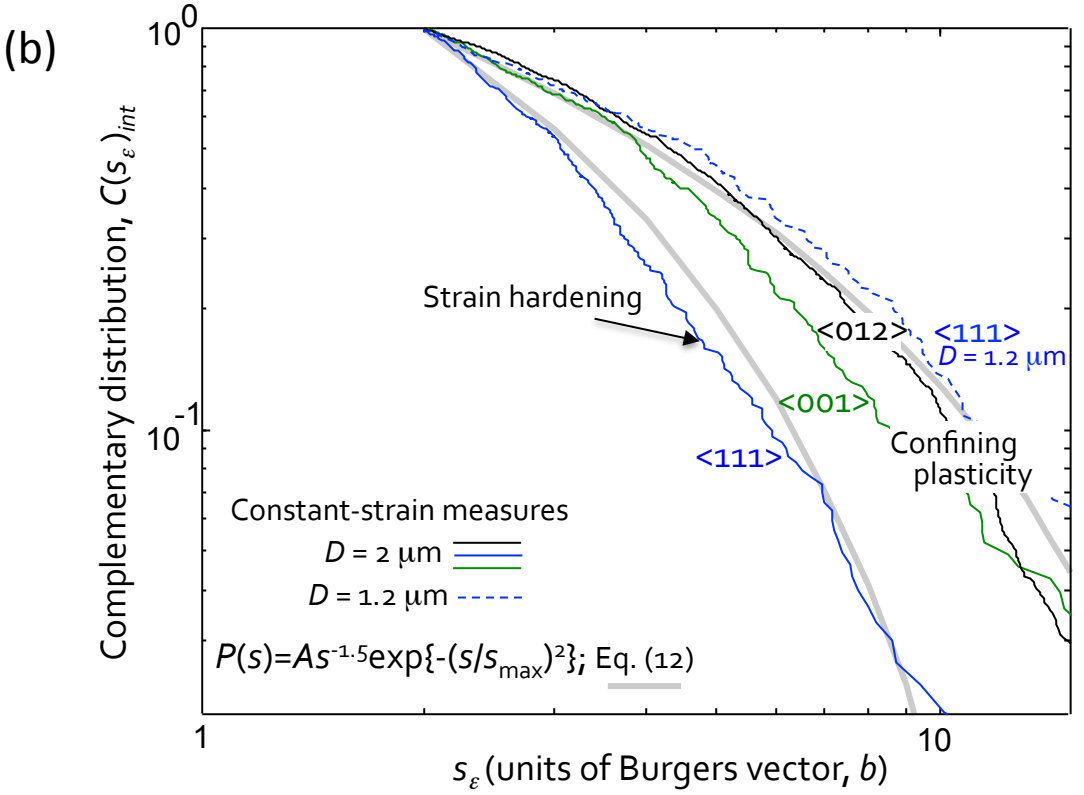

Fig. 8: Stress-integrated complementary cumulative distribution function of avalanche slips s_σ and s_ε. Transition between the microscale strain hardening and confining plasticity domains is illustrated along with the flexibility of Eq. (12) in capturing experimental results. [Experiments used for the <001> orientation lie at the boundary between the plasticity domains, with prevalence of strain hardening.]

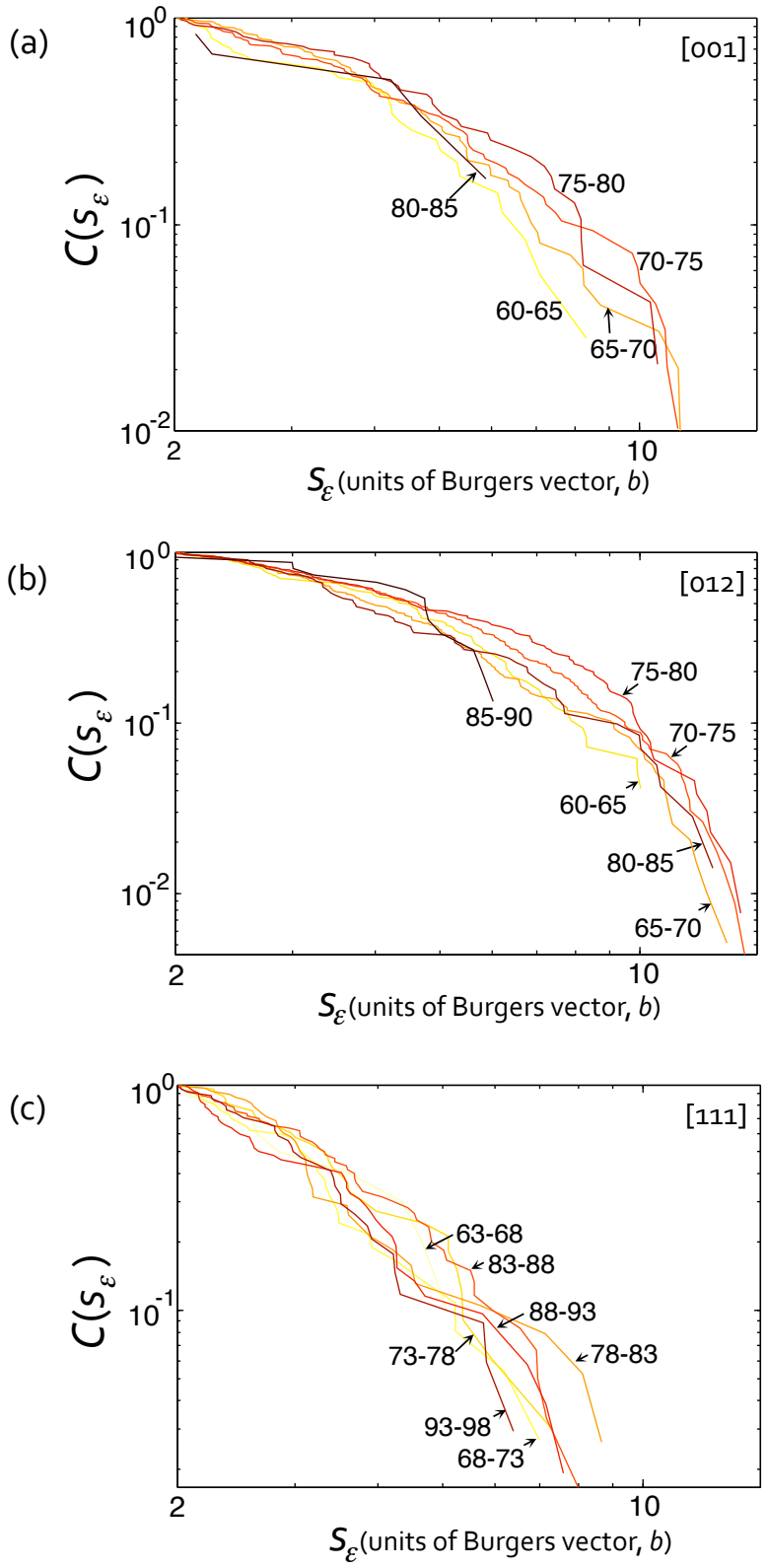

Fig. 9: Stress—binned complementary cumulative distributions $C(s_\varepsilon)$ of dislocation avalanches from the experiments in Fig. (8). The range of applied shear stresses in the active slip systems is given in MPa. Parts (a) and (b) are for micropillars deforming in the confining microscale plasticity regime. Part (c) is for micropillars deforming within the microscale strain hardening domain.

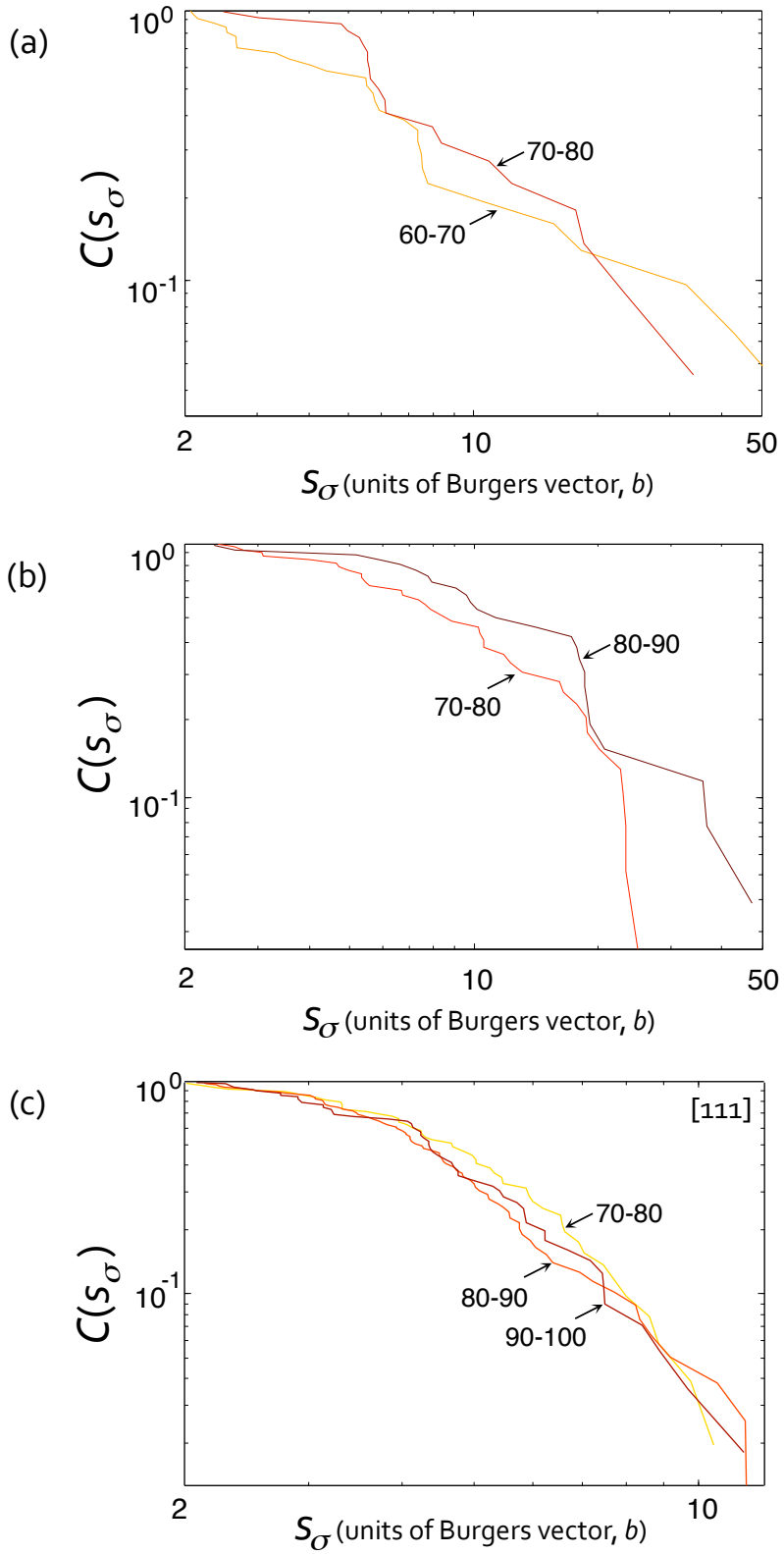

Fig. 10: Stress—binned complementary cumulative distributions $C(s_\sigma)$ for strain increments at constant stress from the experiments in Fig. (8). The range of applied shear stresses in the active slip systems is given in MPa. Parts (a) and (b) are for micropillars deforming in the confining microscale plasticity regime where only a few points are available because of the vanishing slope of the stress—strain curves passed τ_c (see Fig. 1(b)). Part (c) is for micropillars deforming within the microscale strain hardening domain.

Appendix A: Supplementary Online Material

1. Accounting for dislocation cross-slip in microscale strain hardening

The good agreement between experimental stress—strain curves and those predicted from mean-field analysis with configuration C1 can be further improved by accounting for dislocation cross-slip. Within the framework of Eq. (5) from the main text, cross-slip reduces dislocation storage through subtracting term $y\rho^{\alpha}$, so that

$$\frac{d\rho^{\alpha}}{d\gamma^{\alpha}} = \frac{1}{b}\left(\frac{1}{L_{eff}} - y\rho^{\alpha}\right) \quad . \qquad \text{Eq. (A1)}$$

The agreement between experiments and simulations becomes optimum by assuming a critical annihilation distance y = 0.5 nm, which is coincidental with that used in the modeling of dislocation cross-slip in bulk Cu crystals (e.g., [1]). While this is an effective modeling approach, it is recognized that the complexities of double cross-slip [2] and its influence in the development of a three-dimensional dislocation network are beyond the present analysis. It is nevertheless important to note that cross-slip does not affect upon the fundamentals of dislocation interactions as measured through matrix $a_{\alpha\beta}$ in the main text [3].

2. Stability of loading orientation and artifacts from micropillar compression

Present strain-hardening model is implemented in a continuum crystal plasticity finite-element (FE) computational scheme [4], where anisotropic elasticity is accounted for in the analyses and rate-dependent plastic strains are assumed following [5]. This enables assessment of whether the plastic tilting of the micropillar along with the frictional constrains from its top surface would affect inferred stress—strain curves.

Micropillars with the <111> orientation show that for an apparent logarithmic uniaxial strain $\varepsilon = \ln(l_i/l_o) = 5.0 \times 10^{-2}$ –where l_i is the instantaneous pillar length (height) at a given stress level and l_o is the initial pillar length– plastic flow accumulates exclusively along the pillar without any significant strain concentrations occurring at the bottom attachment with the bulk crystal. The bulk remains elastic because in the absence of surface truncated dislocation sources, plastic flow is prevented from occurring. The elastic strains at this attachment are thus vanishingly small and do not contribute to the inferred stress—strain curve. Pillar tilting followed by rotation further occurs for $\varepsilon > 3.0 \times 10^{-2}$ (Fig. A1(a)). This deformation mode arises because of the inducement of asymmetric flow at the bottom attachment with the bulk. By accounting for a small Coulomb's friction coefficient μ = 0.05 between the <111> pillar and the compressing punch, onset of pillar tilting and rotation is however postponed to $\varepsilon > 6 \times 10^{-2}$ (Fig. A1(b)). Tilting and rotation are fully prevented even for $\varepsilon > 0.2$ when μ = 0.30 is imposed (Fig. A1(c)). Complementary simulations finally show that pillar tilting in less significant in the present multiple glide <111> oriented micropillars than in those oriented for single glide.

An important outcome from the above simulations is that whereas the apparent stress—strain curves obtained through micropillar compression experiments in <111> oriented copper crystals may not strictly describe the uniaxial strain hardening response at large uniaxial strain levels, these curves remain accurate to the maximum value of $\varepsilon = 5.0 \times 10^{-2}$ from Fig. 1 in the main text. This is so irrespectively of the assumed of μ.

Finally, one may note that tapering along the pillar length occurs during FIB machining. In the present investigation, the diameter at the top surface of the micropillar was found to be ~ 15% smaller than that at the bottom. In this sense, it is noted that the stress—strain curves in Fig. 1 from the main text where obtained under the assumption of an effective cross-sectional area located at the top 2/3 of the pillar length. Simulations of pillar tapering with the present mean-field strain hardening model showed that this approach is indeed sensible as the apparent uniaxial stress departs in less that 4% from the true value.

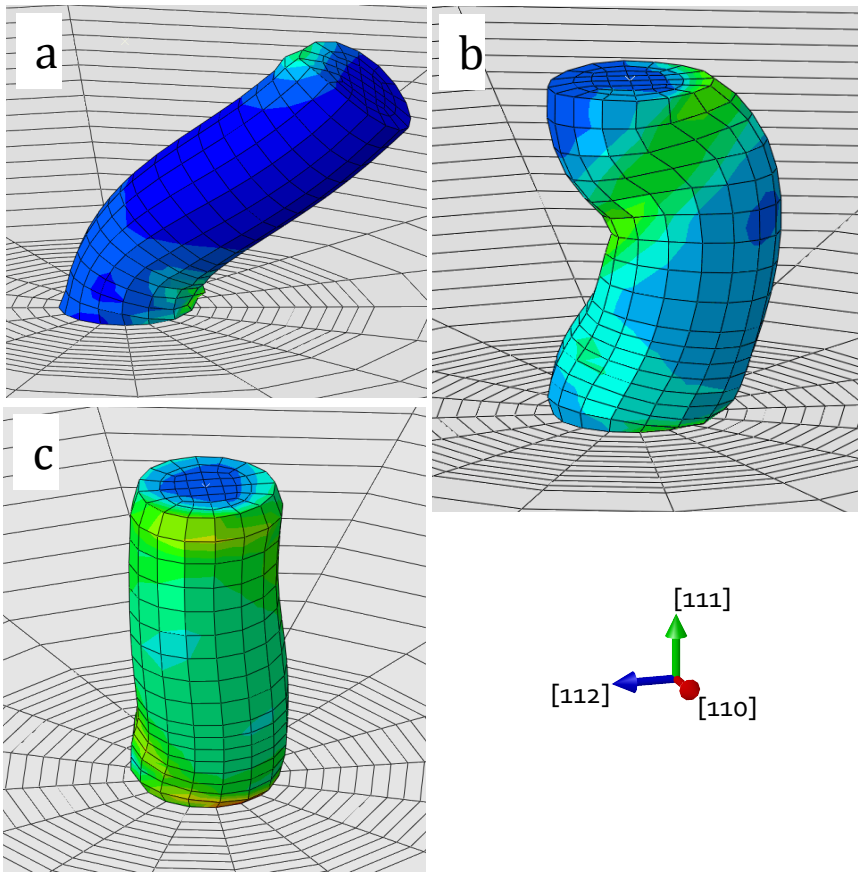

Fig. A1: Influence of mechanical constraints upon micropillar compression experiments from FE simulations for D = 2 μm. Parts (a) and (b) are for a frictionless and frictional contacts (Coulomb's friction coefficient μ = 0.07) with the flat punch compressing the pillar, respectively. Imposed uniaxial strain ε = 0.26. Part (c) is for μ = 0.30 at ε = 0.20 where friction fully prevents pillar tilting. The isocontours are of total shear strain in the slip systems, where green denotes large strains and blue denotes small strains (different scales apply to each snapshot).

3. Mean-field model for the cumulative distribution of dislocation avalanches

Following Eq. (12) in the main text, the probability density of avalanche sizes is given by

$$P(s) = A\, s^{-1.5} \exp\{-(s/s_{\max})^2\} \quad . \qquad \text{Eq. (A2)}$$

By definition, normalization factor A fulfills

$$A^{-1} = \int_{s_{\min}}^{\infty} s^{-3/2} \exp\{-(s/s_{\max})^2\}\, ds \qquad \text{Eq. (A3)}$$

where $s_{\min}$ is the size of the minimum (experimentally discernable) avalanche size. The complementary distribution function then becomes

$$C(s) = 1 - A \int_{s_{\min}}^{s} s^{-3/2} \exp\{-(s/s_{\max})^2\}\, ds \quad . \qquad \text{Eq. (A4)}$$

The analytical solution to this function is plotted in Fig. 8 from the main paper for the values of parameter s_0 best fitting the experimentally measured distributions of slips s_ε and s_σ.

Fig. A2 finally illustrates the distribution of slips s_ε as a function of the applied shear stress, which are used in the computation of the distributions functions in Figs. 8—10 from the main text. It is noted that the mean values of the slip distributions are rather insensitive of the applied stress level, which anticipates the SOC paradigm described in the paper.

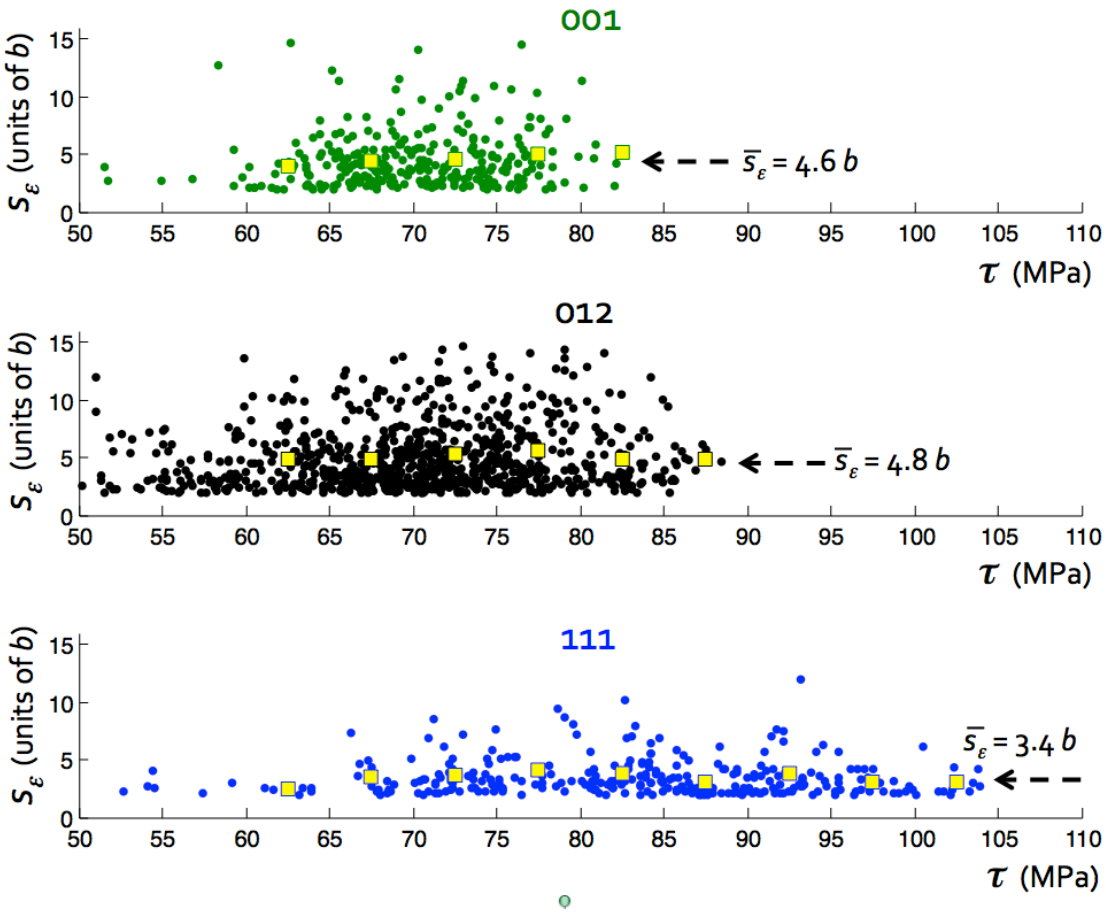

Fig. A2: Statistics of slips s_ε in terms of the resolved shear stress τ in the active slip systems (D = 2 μm). Yellow squares are arithmetic means at fixed values of τ.

References

1. B. Devincre, T. Hoc, L. Kubin. Science **320**, 1745 (2008).

2. S.I. Rao, D.M. Dimiduk, T.A. Parthasarathy, J. El-Awady, C. Woodward, M.D. Uchic, Acta Mater. **59**, 7135 (2011).

3. R. Madec, B. Devincre, L. Kubin, Phys. Rev. Lett. **89**, 255508 (2002).

4. Y. Huang, Mech-178, Division of Applied Sciences. Hardvard University (1991).

5. Rauch, Thèse d'habilitation, Institut National Polytechnique de Grenoble (1993).